

ORIGINAL RESEARCH PAPER

Samarium doped $Mg_{0.33}Ni_{0.33}Co_{0.33}Fe_{2-x}O_4$ Nanoparticles for the Removal of As (III) and Pb (II) Heavy Metal Ions

Mariam Rabaa¹, Amani Aridi^{1*}, Ghassan Younes¹ and Ramadan Awad^{2,3}

¹ Chemistry Department, Faculty of Science, Beirut Arab University, Beirut, Lebanon

² Physics Department, Faculty of Science, Beirut Arab University, Beirut, Lebanon

³ Physics Department, Faculty of Science, Alexandria University, Alexandria, Egypt

Received: 2023-04-11

Accepted: 2023-05-30

Published: 2023-10-14

ABSTRACT

Heavy metal ions, such as As (III) and Pb (II), are harmful even at trace levels and have caused serious health effects on living beings. Therefore, removing these heavy metal ions from the aqueous environment is highly desirable. In this study, $Mg_{0.33}Ni_{0.33}Co_{0.33}Sm_xFe_{2-x}O_4$ nanoparticles, where $x = 0.00, 0.01, 0.02, 0.04, \text{ and } 0.08$, were synthesized by the co-precipitation method and characterized using X-Ray Diffraction (XRD), Transmission Electron Microscopy (TEM) and UV-Vis spectroscopy techniques to study the structural and optical properties. The prepared nanoparticles were applied as adsorbents for the removal of As (III) and Pb (II) from wastewater. Among the prepared samples, $Mg_{0.33}Ni_{0.33}Co_{0.33}Sm_xFe_{2-x}O_4$ nanoparticles with $x = 0.04$ and 0.08 exhibited improved adsorption performance whereas As (III) was removed after 90 min. The experimental adsorption data of As (III) was well fitted with a second-order kinetics model and Langmuir isotherm. Furthermore, the highest removal % of Pb (II) was revealed by $Mg_{0.33}Ni_{0.33}Co_{0.33}Sm_xFe_{2-x}O_4$ nanoparticles with $x = 0.01$. Thus, doping $Mg_{0.33}Ni_{0.33}Co_{0.33}Fe_2O_4$ with Sm improved the adsorption performance of nanoparticles for the removal of As (III) more than that of Pb (II).

Keywords: Spinel ferrite nanoparticles; Heavy metal ions removal; As (III) and Pb (II); second-order kinetics; Langmuir adsorption isotherm.

How to cite this article

Rabaa M., Aridi A., Younes G., Awad R., Samarium doped $Mg_{0.33}Ni_{0.33}Co_{0.33}Fe_2O_4$ Nanoparticles for the Removal of As (III) and Pb (II) Heavy Metal Ions, J. Water Environ. Nanotechnol., 2023; 8(4): 357-368. DOI: 10.22090/jwent.2023.04.003

INTRODUCTION

With the expansion of industry and human activities, such as plating, batteries, pesticides, electroplating, and mining, excessive amounts of heavy metal ions and organic pollutants are found in wastewater [1-3]. Lead (Pb), arsenic (As), mercury (Hg), cadmium (Cd), and chromium (Cr) are the most often used heavy metals [4]. Being non-biodegradable and carcinogenic, the presence of heavy metal ions in water in inappropriate concentration poses a serious risk to the health of all living things [5]. Since heavy metal ions endanger both human health and the ecosystem their removal from water is highly desirable. Consequently, several technologies have been used

to remove heavy metal ions, including adsorption, chemical precipitation, ion exchange, and membrane filtration [6-8]. Among the previously listed techniques, adsorption is one of the most often applied techniques due to its low cost and ease of usage [9, 10].

The majority of adsorbents, used for the removal of heavy metal ions, are difficult to separate after the treatment process since complicated procedures like filtration or centrifugation are required [11]. However, the usage of magnetic adsorbents solves the separation problem since the adsorbents can be simply separated by applying an external magnetic field. Spinel ferrite nanoparticles have been expansively used in various environmental applications such as the degradation of toxic

* Corresponding Authors Email: a.aridi@bau.edu.lb



This work is licensed under the Creative Commons Attribution 4.0 International License.

To view a copy of this license, visit <http://creativecommons.org/licenses/by/4.0/>.

pollutants and the removal of heavy metal ions [12-15]. This is owed to their small particle size, dispersity, large surface area, and magnetic properties that permit their magnetic separation [16]. Khoso et al. reported the following removal efficiencies of 89 % of Cr(VI), 79 % of Pb (II), and 87 % of Cd(II) by $NiFe_2O_4$ nanoparticles [17]. Moreover, Ca-doped $Ni_{0.4}Zn_{0.6}Fe_2O_4$ nano-ferrites removed 98.25 % of Cd and 57% of Cr ions [18].

Doping spinel ferrite nanoparticles with rare earth metals improves their properties [19, 20]. Based on the above background, this work evaluates the adsorption performance of $Mg_{0.33}Ni_{0.33}Co_{0.33}Sm_xFe_{2-x}O_4$ nanoparticles where $x = 0.00, 0.01, 0.02, 0.04, \text{ and } 0.08$ for the removal of As (III) and Pb (II).

METHODS AND MATERIALS

Synthesis of Nanoparticles

$Mg_{0.33}Ni_{0.33}Co_{0.33}Sm_xFe_{2-x}O_4$ nanoparticles, where $x = 0.00, 0.01, 0.02, 0.04, \text{ and } 0.08$, were synthesized by the co-precipitation technique. Appropriate amounts of $CoCl_2 \cdot 6H_2O$, $NiCl_2 \cdot 6H_2O$, $MgCl_2 \cdot 6H_2O$, $SmCl_3 \cdot 6H_2O$, and $FeCl_3 \cdot 6H_2O$ were dissolved in a specific volume of deionized water. To prepare 25 g of $Mg_{0.33}Ni_{0.33}Co_{0.33}Fe_2O_4$ nanoparticles, 2.58, 2.59, 2.21, and 17.6 g of $CoCl_2 \cdot 6H_2O$, $NiCl_2 \cdot 6H_2O$, $MgCl_2 \cdot 6H_2O$, and $FeCl_3 \cdot 6H_2O$, respectively, were dissolved in deionized water. For the synthesis of $Mg_{0.33}Ni_{0.33}Co_{0.33}Sm_xFe_2O_4$ nanoparticles where $0.01 \leq x \leq 0.08$, the amount of $SmCl_3 \cdot 6H_2O$ and $FeCl_3 \cdot 6H_2O$ ranges between 0.06 and 0.47 g and between 8.38 and 8.76 g, respectively. Then, the prepared solutions were mixed and stirred magnetically for 30 minutes at room temperature. Afterward, 60 g of sodium hydroxide (NaOH) was dissolved in 0.5 L of deionized water to prepare a 3 M solution of NaOH which was added to the mixture drop by drop till reaching pH 12. Then, while stirring magnetically, the resulting solution was heated at 80 °C for 2 hours. The precipitated products were filtered and washed until the pH reached 7. The precipitates were dried for approximately 18 hours at 100 °C. Finally, dried powders were then annealed at 550 °C for 4 hours.

Characterization of $Mg_{0.33}Ni_{0.33}Co_{0.33}Sm_xFe_{2-x}O_4$ Nanoparticles

The structural properties of the prepared samples were determined by X-ray diffraction (XRD) and transmission electron microscopy

(TEM). Thus, Bruker D8 Focus was employed to do the XRD analysis using $Cu\text{-}k_\alpha$ radiation source ($\lambda = 1.54056 \text{ \AA}$) in the range of $20^\circ \leq 2\theta \leq 80^\circ$. The morphology and particle size were evaluated by TEM via JEM-1400 Plus. The optical properties of the prepared samples were evaluated by ultraviolet-visible (UV-Vis) spectroscopic measurements that were conducted in the range of 290 - 700 nm using a V-670 spectrophotometer. The magnetic properties were examined at room temperature by a Lakeshore 7410 vibrating sample magnetometer (VSM) applying a magnetic field in the range of -20000 and +20000 G.

Adsorption Performance of $Mg_{0.33}Ni_{0.33}Co_{0.33}Sm_xFe_{2-x}O_4$ Nanoparticles

The adsorption performance of $Mg_{0.33}Ni_{0.33}Co_{0.33}Sm_xFe_{2-x}O_4$ nanoparticles, where $0.00 \leq x \leq 0.08$, was evaluated for the removal of As (III) and Pb (II). The desired concentrations of the As (III) and Pb (II) solutions, namely 5 $mg \cdot L^{-1}$ for As (III) and 5, 7.5, and 10 $mg \cdot L^{-1}$ for Pb (II), were prepared through dilution of the corresponding stock solutions. It is important to note that the stock solutions for As (III) and Pb (II), purchased from Sigma-Aldrich, have a concentration of 1000 $mg \cdot L^{-1}$ each. The pH of 5 $mg \cdot L^{-1}$ As (III) and Pb (II) solutions are 2.69 and 2.64, respectively. To determine the most efficient sample in the removal of As (III) and Pb (II), 40 mg of each of the prepared samples was mixed with 50 mL of 5 $mg \cdot L^{-1}$ As (III) and Pb (III) solutions. The mixtures were sonicated at room temperature. After a predetermined time interval, the concentration of heavy metal ions was determined by atomic absorption spectroscopy (AAS). The adsorption kinetics and isotherm for the removal of As (III) were determined. Furthermore, the effect of the adsorbent amount and initial concentration of Pb (II) on the removal % of Pb (II) was studied. The removal % and adsorption capacity (q_e) were calculated using the following formulas:

$$\text{Removal \%} = \frac{C_0 - C_t}{C_0} \times 100 \quad \text{and} \quad (1)$$

$$q_e = \frac{(C_0 - C_e) \times V}{m}, \quad (2)$$

where C_0 ($mg \cdot L^{-1}$) and C_e ($mg \cdot L^{-1}$) denote the concentration of As (III) at $t = 0$ and equilibrium respectively, V (L) is the volume of As (III) solution, and m (g) is the adsorbent mass.

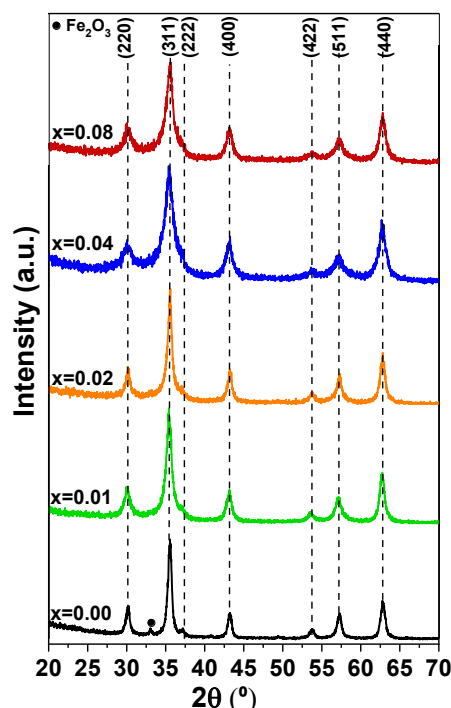


Fig. 1 XRD patterns of $Mg_{0.33}Ni_{0.33}Co_{0.33}Sm_xFe_{2-x}O_4$ nanoparticles $x = 0.08$.

Table 1 The values of lattice parameter (a), X-ray density (ρ), and specific surface area (S) of $Mg_{0.33}Ni_{0.33}Co_{0.33}Sm_xFe_{2-x}O_4$ nanoparticles with $x = 0.08$

x	a (Å)	$\rho \times 10^3$ (kg/m ³)	S (m ² /g)
0.00	8.351	5.075	41.164
0.01	8.372	5.059	45.469
0.02	8.361	5.101	45.290
0.04	8.437	5.006	54.356
0.08	8.380	5.194	53.335

RESULTS AND DISCUSSION

Structural, Optical, and Magnetic Properties of $Mg_{0.33}Ni_{0.33}Co_{0.33}Sm_xFe_{2-x}O_4$ Nanoparticles

The XRD patterns for $Mg_{0.33}Ni_{0.33}Co_{0.33}Sm_xFe_{2-x}O_4$ nanoparticles where $0.00 \leq x \leq 0.08$ are displayed in Fig. 1. The observed peaks are indexed to cubic spinel phase with space group $Fd\bar{3}m$ and are well matched with the standard JCPDS card no. 36-0398 [21]. The presence of an extra peak in the XRD pattern confirms the presence of hematite as a secondary phase. However, the intensity of this peak decreases as the Sm content increases. The decrease in intensity of the hematite peak might be attributed to the occupation of Sm^{3+} ions in the host lattice. Thus, the absence of extra peaks of dopants or secondary phases revealed

the successful replacement of iron ions by the dopant ions (Sm^{3+}). Similar results are reported in a previous study upon doping $Co_{0.9}Cu_{0.1}Fe_2O_4$ with Dy^{3+} and Sm^{3+} [22]. The lattice parameter (a) values of $Mg_{0.33}Ni_{0.33}Co_{0.33}Sm_xFe_{2-x}O_4$ nanoparticles where $0.01 \leq x \leq 0.08$ are greater than that of pure nanoparticles ($x = 0.00$) as listed in Table 1. This is mainly attributed to the substitution of Fe^{3+} by Sm^{3+} ions which is driven by the significant difference in ionic radii knowing that Sm^{3+} ions have a larger ionic radius (1.08 Å) compared to that of Fe^{3+} (0.65 Å). Liu et al. [23] reported similar results where the lattice parameter increased from 8.381 to 8.411 Å upon doping $Ni_{0.5}Zn_{0.5}Fe_2O_4$ with Sm.

TEM images and particle size distribution of $Mg_{0.33}Ni_{0.33}Co_{0.33}Sm_xFe_{2-x}O_4$ nanoparticles are

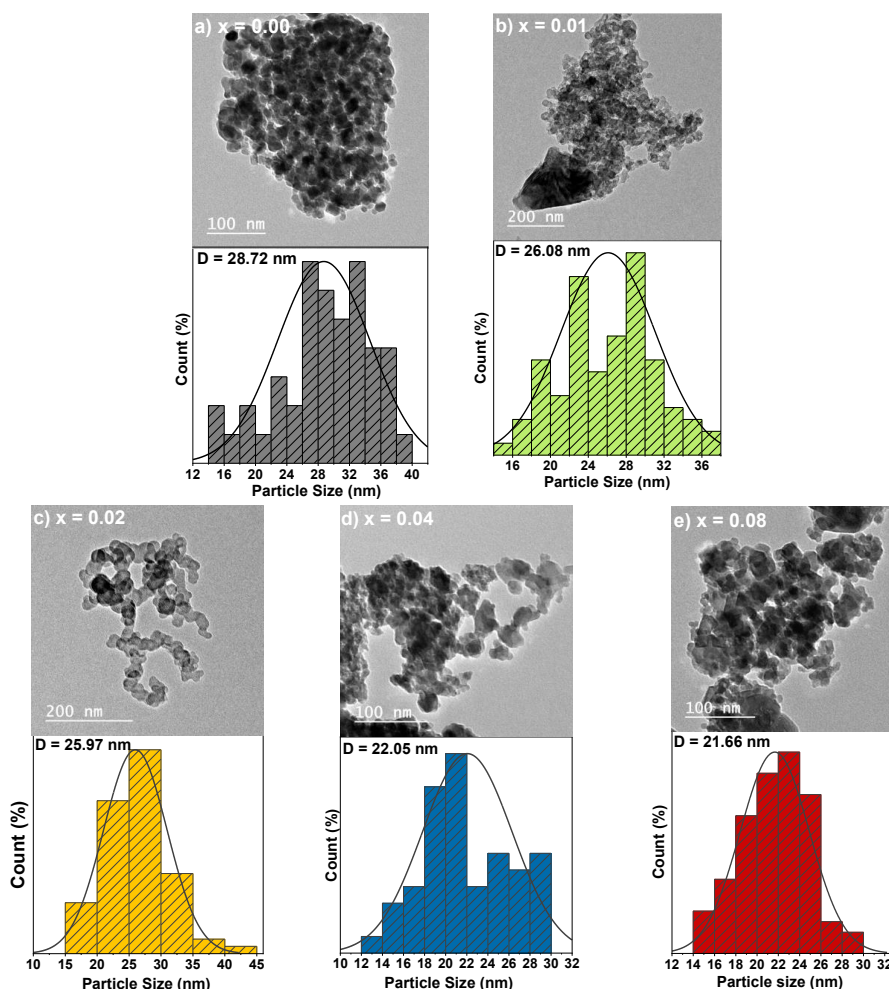


Fig. 2 TEM images and particle size distribution of $Mg_{0.33}Ni_{0.33}Co_{0.33}Sm_xFe_{2-x}O_4$ nanoparticles where (a) $x = 0.00$, (b) $x = 0.01$, (c) $x = 0.02$, (d) $x = 0.04$ and (e) $x = 0.08$.

displayed in Fig. 2. The prepared samples exhibit spherical morphology. In addition, as Sm content rises from 0.00 to 0.08, the average particle size is reduced from 28.72 to 21.66 nm. It is known that the rare earth metal ions substitution shrinks the particle size of ferrite nanoparticles as reported in previously published studies [24, 25]. The particle size reduction is attributed to the substitution of Fe^{3+} with Sm^{3+} . The diffusion of Sm^{3+} , having a larger ionic radius than Fe^{3+} , into $Mg_{0.33}Ni_{0.33}Co_{0.33}Fe_2O_4$ grains arises upon doping nanoparticles with Sm. Thus, the surface energy is reduced and the growth of the nanoparticles is inhibited owed to the segregation of Sm^{3+} to the surface. Similar results were reported in a previous study where the particle size was reduced from 60 to 32 nm as the Sm content increased from 0 to 0.1 in $CoSm_xFe_2$.

xO_4 nanoparticles [26].

The specific surface area of nanoparticles plays a vital role in their versatility and applicability across various fields such as catalysis and heavy metal adsorption. To determine the specific surface area (S) of the synthesized nanoparticles, the following relation was employed [27]:

$$S = \frac{6000}{\rho \times D}, \quad (3)$$

where ρ and D represent the X-ray density and the average particle size obtained from TEM analysis, respectively. It is worth mentioning that the X-ray density (ρ) was calculated using the following equation [27]:

$$\rho = \frac{8M}{N_A \times a^3}, \quad (4)$$

knowing that M denotes the molar mass, N_A represents Avogadro's number, and a signifies the lattice parameter of the prepared nanoparticles. The obtained values of ρ and S are listed in Table 1. Notably, the specific surface area (S) increases upon doping nanoparticles with Sm. Among the prepared samples, $Mg_{0.33}Ni_{0.33}Co_{0.33}Sm_xFe_{2-x}O_4$ nanoparticles with $x = 0.04$ exhibited the largest specific surface area ($S = 54.356 \text{ m}^2/\text{g}$)

The optical properties of $Mg_{0.33}Ni_{0.33}Co_{0.33}Sm_xFe_{2-x}O_4$ nanoparticles, where x ranges between 0.00 and 0.08, are determined via UV-vis spectroscopy. The absorption spectra, depicted in Fig. 3, were recorded in the range of 290 - 700 nm and a major peak appeared at 335 nm. Comparable UV spectra of $Ni_{1-x}Mg_xFe_2O_4$ nanoparticles are stated in previous studies [28].

The bandgap energy (E_g) was estimated from Tauc's plot by applying the following equation:

$$(\alpha h\nu)^2 = A (h\nu - E_g), \quad (5)$$

where α denotes the absorption coefficient, $h\nu$ is the photon energy and A represents the transition probability constant. Thus, the bandgap energy (E_g) was assessed by plotting $(\alpha h\nu)^2$ versus $h\nu$, as displayed in Fig. 4 and Table 2. The Sm-doped nanoparticles revealed greater E_g values compared to that of pure $Mg_{0.33}Ni_{0.33}Co_{0.33}Sm_xFe_{2-x}O_4$ ($x=0.00$). As revealed from TEM analysis, the Sm-doped samples revealed smaller particle sizes compared with pure nanoparticles. Thus, the decrease in the particle size and increase in the bandgap energy upon Sm-doping is owed to the quantum size effect [29].

The Urbach energy (E_U), related to the disorder or defect in the prepared samples, is estimated from the following equation:

$$\ln(\alpha) = \ln(\alpha_0) + \frac{h\nu}{E_U}, \quad (6)$$

knowing that α_0 is constant. Thus, E_U is determined from the reciprocal slope of the plot of $\ln(\alpha)$ vs. $(h\nu)$. The obtained results are displayed in Fig. 5 and E_U values are listed in Table 2. The doped samples exhibited lower E_U than pure nanoparticles. Furthermore, an inverse proportionality between E_U and E_g was noticed. Similar results were reported in a previous study upon doping $ZnFe_2O_4$ and thin films of PVA with La and $SrCuTi_2Fe_{14}O_{27}$, respectively [30, 31].

The extinction coefficient (k) related to the absorption coefficient (α) can be determined by the

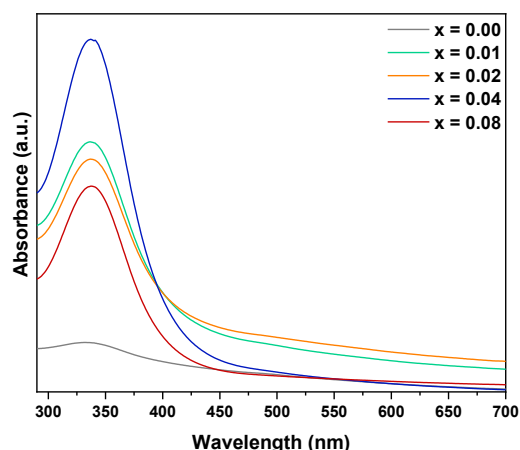


Fig. 3 UV-vis spectra of $Mg_{0.33}Ni_{0.33}Co_{0.33}Sm_xFe_{2-x}O_4$ nanoparticles with x 0.08.

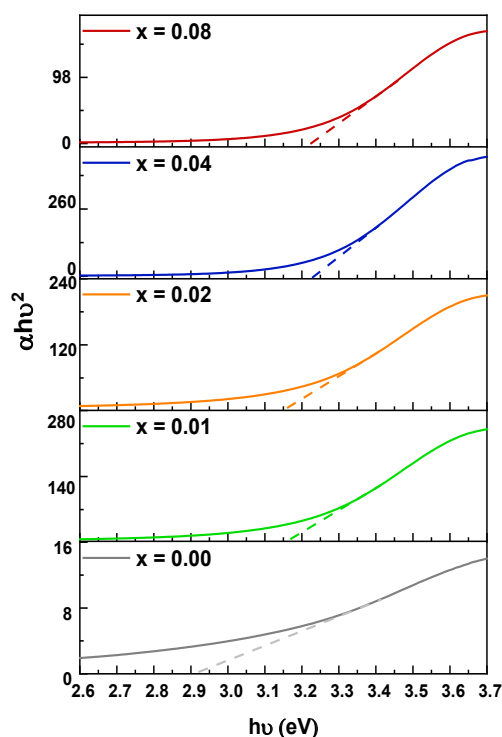


Fig. 4 Tauc's plot of $Mg_{0.33}Ni_{0.33}Co_{0.33}Sm_xFe_{2-x}O_4$ nanoparticles with x 0.08.

Table 2 Bandgap energy (E_g) and Urbach energy (E_U) values of $Mg_{0.33}Ni_{0.33}Co_{0.33}Sm_xFe_{2-x}O_4$ nanoparticles with x 0.08

x	E_g (eV)	E_U (eV)
0.00	2.915	1.322
0.01	3.172	0.517
0.02	3.157	0.555
0.04	3.234	0.331
0.08	3.215	0.365

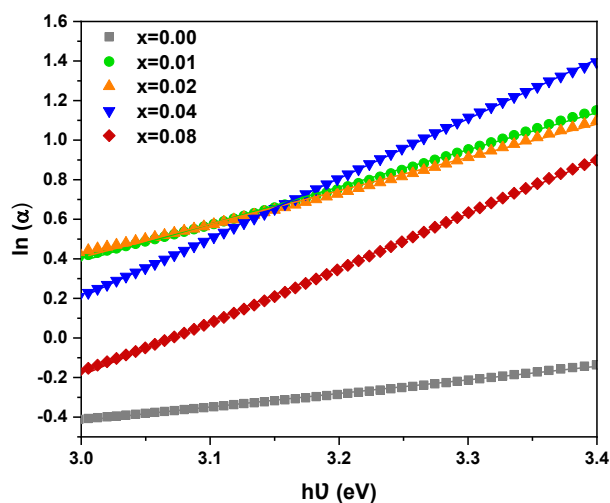


Fig. 5 Plots of E_U determination of $Mg_{0.33}Ni_{0.33}Co_{0.33}Sm_xFe_{2-x}O_4$ nanoparticles with $x = 0.08$.

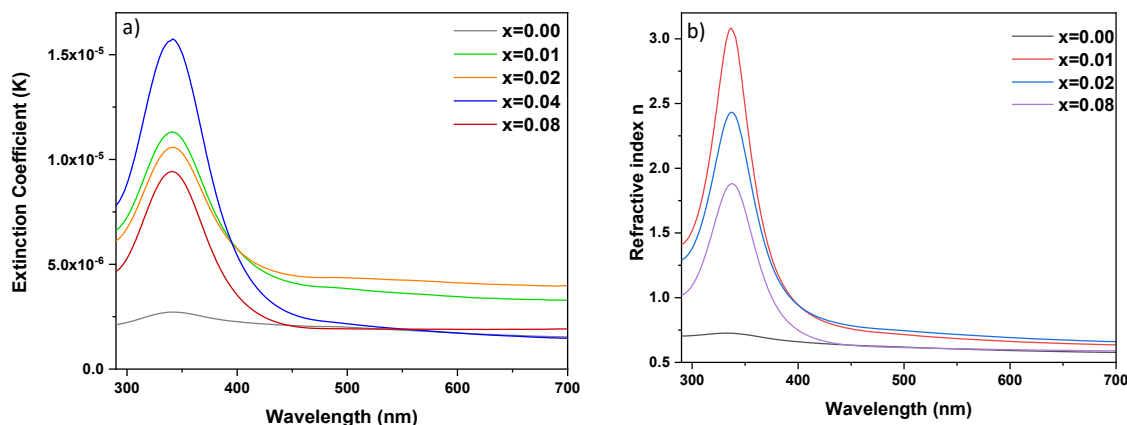


Fig. 6 Variation of the (a) extinction coefficient (k) and (b) refractive index against wavelength for $Mg_{0.33}Ni_{0.33}Co_{0.33}Sm_xFe_{2-x}O_4$ nanoparticles with $x = 0.08$.

following equation [30]:

$$k = \frac{\alpha \lambda}{4\pi} \tag{7}$$

The variation of the extinction coefficient (k) as a function of wavelength (λ) for the prepared samples is illustrated in Fig. 6 (a). The extinction coefficient (k) increases to its maximum value around 335 nm and then decreases. Furthermore, the extinction coefficient of Sm-doped samples is greater than that of pure nanoparticles. This might be attributed to the increase in the absorption coefficient revealing the occurrence of direct electronic transitions [30, 32].

The refractive index (n) is an important characteristic in determining the optical and electric properties of a semiconductor [33]. It can

be calculated from the following equation:

$$n = \frac{1}{T_s} + \left(\frac{1}{T_s - 1} \right)^{1/2} \tag{8}$$

where T_s is the percentage transmission coefficient. The variation of the refractive index (n) against wavelength for $Mg_{0.33}Ni_{0.33}Co_{0.33}Sm_xFe_{2-x}O_4$ nanoparticles with $0.00 \leq x \leq 0.08$ is represented in Fig. 6 (b). The refractive index increases as the wavelength increases to reach 335 nm. With a further increase in the wavelength to reach 700 nm, the refractive index decreases. Furthermore, the refractive index is greatly increased upon doping the nanoparticles with Sm. Hence, doping $Mg_{0.33}Ni_{0.33}Co_{0.33}Sm_xFe_{2-x}O_4$ nanoparticles plays



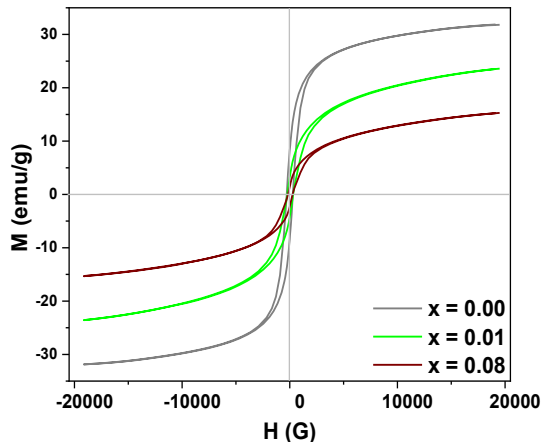


Fig. 7. M-H loops of $Mg_{0.33}Ni_{0.33}Co_{0.33}Sm_xFe_{2-x}O_4$ nanoparticles with $x = 0.00, 0.01$ and 0.08 .

an important role in controlling the k and n values, helps in enhancing the optical properties of nanomaterials and enables its usage in optoelectronic applications [30].

The prepared nanoparticles were subjected to VSM analysis to investigate their magnetic properties. The obtained M-H loops are displayed in Fig. 7. Ferromagnetic behavior was exhibited by $Mg_{0.33}Ni_{0.33}Co_{0.33}Sm_xFe_{2-x}O_4$ nanoparticles with $x = 0.00, 0.01$ and 0.08 . Furthermore, the values of M_s and M_r are reduced from 31.87 to 15.31 emu/g and from 8.31 to 1.72 emu/g, respectively, as Sm content increases from 0.00 to 0.08. In addition, the H_c values are reduced from 284.89 to 199.70 G upon doping nanoparticles with Sm. The reduction in M_s and M_r can be attributed to the introduction of Sm^{3+} ions into the nano ferrite lattice, which replaces some of the Fe^{3+} ions. This substitution leads to a dilution of the magnetic moment, as the magnetic moment of Sm^{3+} (1.7 μB) is smaller than that of Fe^{3+} (5 μB) [34]. Consequently, the overall magnetic moment of the doped nanoparticles decreases, resulting in a decrease in the M_s values.

Adsorption Performance of Nanoparticles for the Removal of As (III)

The efficiency of $Mg_{0.33}Ni_{0.33}Co_{0.33}Sm_xFe_{2-x}O_4$ nanoparticles with $0 \leq x \leq 0.08$ for the removal of As (III) was evaluated. The removal % of As (III) as a function of contact time in the presence of nanoparticles with various Sm content is shown in Fig. 8. As the contact time increases from 30 to 90 min, the removal % of As (III) increases. Among the prepared samples, $Mg_{0.33}Ni_{0.33}Co_{0.33}Sm_xFe_{2-x}O_4$

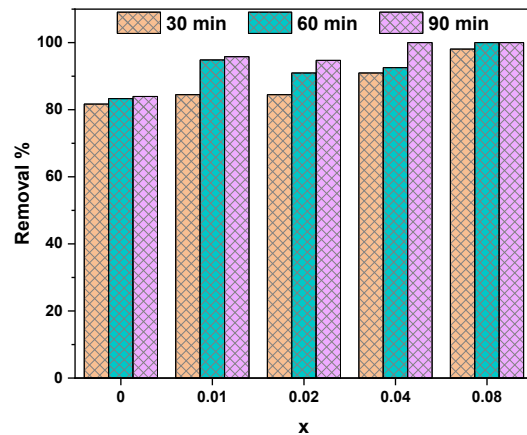


Fig. 8. Removal % of As (III) in the presence of 40 mg of $Mg_{0.33}Ni_{0.33}Co_{0.33}Sm_xFe_{2-x}O_4$ nanoparticles with $x = 0.08$ after a contact time of 30, 60, and 90 min analyzed at room temperature.

nanoparticles with $x = 0.04$ and 0.08 exhibited improved performance where 100 % of As (III) was removed after 90 min. Thus, the adsorption activity of $Mg_{0.33}Ni_{0.33}Co_{0.33}Fe_2O_4$ nanoparticles is boosted with Sm doping. Enhanced adsorption performance was exhibited by $Mg_{0.33}Ni_{0.33}Co_{0.33}Sm_xFe_{2-x}O_4$ nanoparticles with $x = 0.04$ and 0.08 compared with magnetite-maghemite nanoparticles; 98.5 % of As (III) was removed in the presence of 0.4 $g.L^{-1}$ of magnetite-maghemite nanoparticles after a contact time of 24 hours knowing that the starting initial As (III) concentration was 1.5 mg/L and the solution $pH = 2$ [35].

Adsorption kinetics

To study the adsorption kinetics, 40 mg of $Mg_{0.33}Ni_{0.33}Co_{0.33}Sm_xFe_{2-x}O_4$ nanoparticles with $0 \leq x \leq 0.08$ was mixed with 50 mL of 5 $mg.L^{-1}$ As (III) solution having $pH = 2.69$. The adsorption kinetics were analyzed at room temperature. To determine the kinetic model that best fits the adsorption experimental results of As (III), the first-order, second-order, Elovich, and intra-particle diffusion (IPD) models were applied. The first-order model is represented in the following equation:

$$\ln (q_e - q_t) = -k_1 t + \ln (q_e). \quad (9)$$

However, the second-order model is represented as follows [36]:

$$\frac{t}{q_t} = \frac{1}{q_e} t + \frac{1}{k_2 q_e^2}, \quad (10)$$

where q_t and q_e represent the adsorption capacity at any time t and equilibrium ($mg.g^{-1}$), k_1 denotes the first-order rate constant (min^{-1})

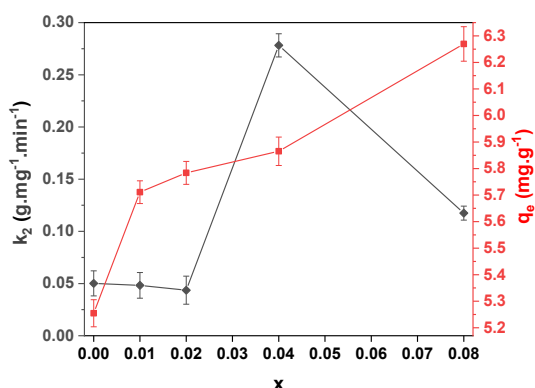


Fig. 9 Rate constant (k_2) and the adsorption capacity at equilibrium (q_e) for the adsorption of As (III) in the presence of 40 mg of $Mg_{0.33}Ni_{0.33}Co_{0.33}Sm_xFe_{2-x}O_4$ nanoparticles with x 0.08 studied at room temperature. Operating conditions for As (III) solution ($V = 50$ mL, $C = 5$ mg.L⁻¹ and $pH = 2.69$).

and k_2 represents the second-order rate constant (g.mg⁻¹.min⁻¹). The Elovich kinetic model is an empirical equation used to describe the adsorption kinetics and assumes that the rate of adsorption is influenced by both the surface coverage and the activation energy of the adsorption process. The Elovich equation can be written as [37]:

$$q_t = \frac{1}{\beta} \times \ln(\alpha\beta) + \frac{1}{\beta} \times \ln(t), \quad (11)$$

where q_t is the amount of solute adsorbed at time t , β is the desorption constant, which represents the desorption energy or activation energy of the adsorption process and α is the initial adsorption rate constant. The intra-particle diffusion (IPD) model, is used to analyze the adsorption process and assumes that the adsorption occurs in multiple stages, including external mass transfer, intra-particle diffusion, and equilibrium. The IPD model can be represented by the equation [38]:

$$q_t = k \times t^{1/2} + I \quad (12)$$

where k represents the IPD rate constant and I is the IPD model's boundary layer constant.

The equations and the coefficient of determination values (R^2) of the kinetics fitting data are listed in Table 3. The R^2 values were found to be close to 1 by applying the second-order kinetics model and are much greater than that obtained by applying the first-order kinetics, Elovich, and Intra-particle diffusion models. This recommends that the second-order model is more satisfactory in describing the adsorption kinetics of As (III). The values of k_2 and q_e were estimated from the

intercept and slope of the linear plot of t/q_t versus t , respectively. The results are displayed in Fig. 9. It is clear that as the Sm dopant content increases from 0.01 to 0.08, the adsorption capacity increases. Furthermore, the highest adsorption rate was achieved in the presence of $Mg_{0.33}Ni_{0.33}Co_{0.33}Sm_xFe_{2-x}O_4$ nanoparticles with $x = 0.04$.

Adsorption Isotherm

The adsorption performance between the As (III) and $Mg_{0.33}Ni_{0.33}Co_{0.33}Sm_{0.04}Fe_{1.96}O_4$ adsorbent can be determined by analyzing the adsorption isotherm. To do so, 40 mg of $Mg_{0.33}Ni_{0.33}Co_{0.33}Sm_{0.04}Fe_{1.96}O_4$ nanoparticles were mixed with As (III) solution ($V = 50$ mL, $C = 5$ mg.L⁻¹ and $pH = 2.69$) at room temperature. Consequently, Langmuir, Temkin, and Freundlich isotherms were applied and the results are shown in Fig. 10. According to the Langmuir isotherm, each active site may only adsorb one molecule, and no interaction exists between adsorbate molecules occupying various active sites. The equation of the Langmuir isotherm is expressed as follows [39]:

$$\frac{C_t}{q_t} = \frac{C_t}{q_{max}} + \frac{1}{q_{max}K_L}, \quad (13)$$

where C_t (mg.L⁻¹) signifies the As (III)

concentration determined in the solution at any time t , q_{max} and q_t (mg.g⁻¹) is the maximum adsorption capacity and the adsorption capacity at any time t , and K_L (L.mg⁻¹) represents the Langmuir constant. The Temkin model, which considers the adsorbate-adsorbent interaction throughout the adsorption process, is expressed by the following equation [40]:

$$q_t = \beta \ln C_t + \beta \ln K_T, \quad (14)$$

knowing that β is the coefficient linked to the sorption heat and K_T is the Temkin equilibrium constant consistent with the maximum binding energy. Whereas, the Freundlich isotherm describes multilayer adsorption as well as interaction amongst the molecules that have been adsorbed. The linearized equation of this model is represented below [41]:

$$\ln q_t = \frac{1}{n} \ln C_t + \ln K_F, \quad (15)$$

where n and K_F symbolize the adsorption intensity and Freundlich constant, respectively. The negative slopes of the plots demonstrating



Table 3 Equations and coefficient of determination (R^2) of first-order, second-order kinetics, Elovich, and Intra-particle diffusion model

x	First-order kinetics		Second-order kinetics		Elovich model		Intra-particle diffusion model	
	Equation	R^2	Equation	R^2	Equation	R^2	Equation	R^2
0.00	$y = -0.03x + 0.37$	0.9436	$y = 0.19x + 0.07$	0.999	$y = 0.65x + 2.31$	0.869	$y = 0.26x + 2.72$	0.686
0.01	$y = -0.03x + 0.57$	0.8065	$y = 0.18x + 0.63$	0.989	$y = 0.82x + 2.11$	0.889	$y = 0.49x + 2.15$	0.908
0.02	$y = -0.03x + 0.67$	0.9132	$y = 0.17x + 0.68$	0.985	$y = 1.02x + 1.43$	0.859	$y = 0.54x + 1.89$	0.945
0.04	$y = -0.05x + 0.21$	0.7678	$y = 0.17x + 0.07$	0.999	$y = 0.17x + 5.13$	0.883	$y = 0.44x + 3.31$	0.566
0.08	$y = -0.02x + 0.27$	0.7847	$y = 0.16x + 0.22$	0.999	$y = 0.39x + 4.57$	0.925	$y = 0.44x + 3.46$	0.711

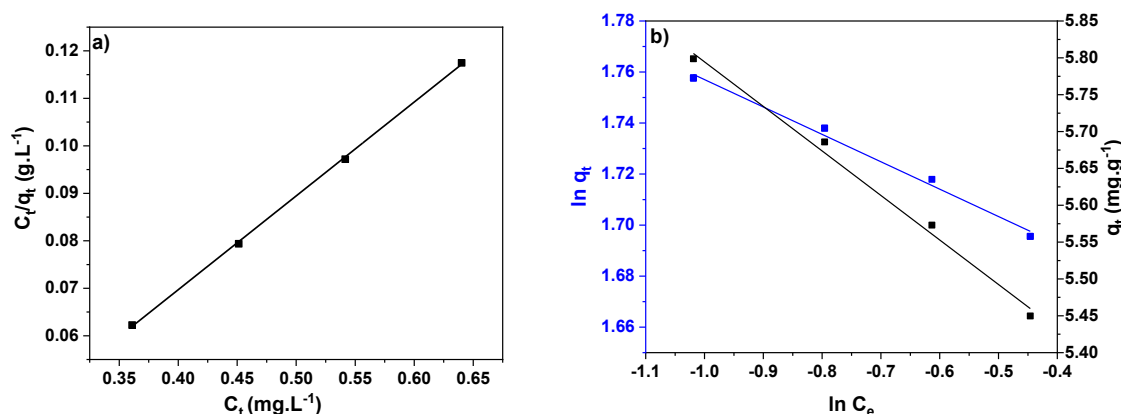


Fig. 10 (a) Langmuir isotherm, and (b) Freundlich and Temkin isotherm plots for adsorption of As (III) in the presence of 40 mg of $Mg_{0.33}Ni_{0.33}Co_{0.33}Sm_{0.04}Fe_{1.96}O_4$ adsorbent examined at room temperature. Operating conditions for As (III) solution ($V = 50$ mL, $C = 5$ $mg.L^{-1}$ and $pH = 2.69$).

Temkin and Freundlich isotherms (Fig. 10 (b)) indicate the failure of these isotherms in the description of the adsorption process of As (III) on $Mg_{0.33}Ni_{0.33}Co_{0.33}Sm_{0.04}Fe_{1.96}O_4$ nanoparticles. However, the linear plot denoting the Langmuir model, represented in Fig. 10 (a), shows the well-fitting of this model with the experimental adsorption data. Thus, q_{max} and K_L , estimated from the slope and intercept of the Langmuir plot, are 5.05 $mg.g^{-1}$ and 0.198 $L.mg^{-1}$. As reported in a previous study, the removal of As (III) using copper II oxide nanoparticles followed the Langmuir model where q_{max} was 1.0862 $mg.g^{-1}$ [42]. Thus, superior activity was revealed by $Mg_{0.33}Ni_{0.33}Co_{0.33}Sm_{0.04}Fe_{1.96}O_4$ nanoparticles in comparison to copper II oxide nanoparticles, as both exhibited conformity with the Langmuir isotherm.

Adsorption Performance of Nanoparticles for the Removal of Pb (II)

To evaluate the performance of $Mg_{0.33}Ni_{0.33}Co_{0.33}Sm_xFe_{2-x}O_4$ nanoparticles with $0 \leq x \leq 0.08$ for Pb (II) removal, the removal % of Pb

(II) was estimated in the presence of 40 mg of each of the prepared nanoparticles after 120 min at room temperature. 50 mL of 5 $mg.L^{-1}$ Pb (II) solution having a pH of 2.64 was used in this experiment. As shown in Fig. 11, the highest removal % is exhibited by $Mg_{0.33}Ni_{0.33}Co_{0.33}Sm_xFe_{2-x}O_4$ nanoparticles with $x = 0.01$.

Effect of adsorbent amount

To investigate the effect of the adsorbent amount on the removal % of Pb (II), different masses of $Mg_{0.33}Ni_{0.33}Co_{0.33}Sm_{0.01}Fe_{1.99}O_4$ nanoparticles (20, 40, 60, and 80 mg) were mixed with 5 $mg.L^{-1}$ Pb (II) solution and the removal % was calculated after 30, 60 and 90 min. The obtained results are shown in Fig. 12 (a). As the contact time between the Pb (II) solution and the adsorbent increases, the removal % also increases. In addition, the removal of Pb (II) is boosted in the presence of 80 mg of adsorbent compared to that in the presence of fewer amounts where 96 % of Pb (II) is removed after 90 min. Thus, increasing the amount of nanoparticles increases the removal of Pb (II). This is mainly attributed to



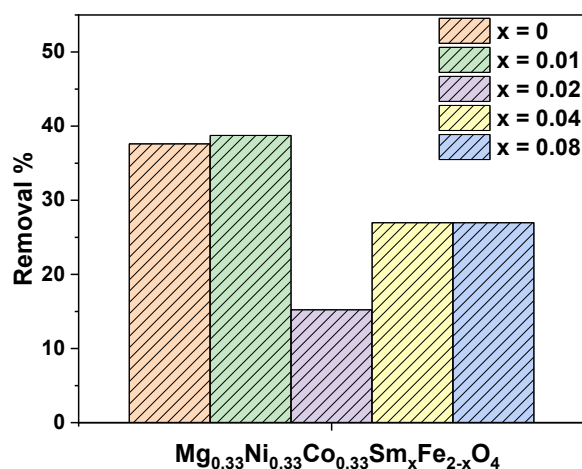


Fig. 11 Removal % of Pb (II) in the presence of 40 mg of $Mg_{0.33}Ni_{0.33}Co_{0.33}Sm_xFe_{2-x}O_4$ nanoparticles with x 0.08 after a contact time of 120 min examined at room temperature (Pb (II) concentration: $5\text{ mg}\cdot\text{L}^{-1}$ volume: 50 mL, pH = 2.64).

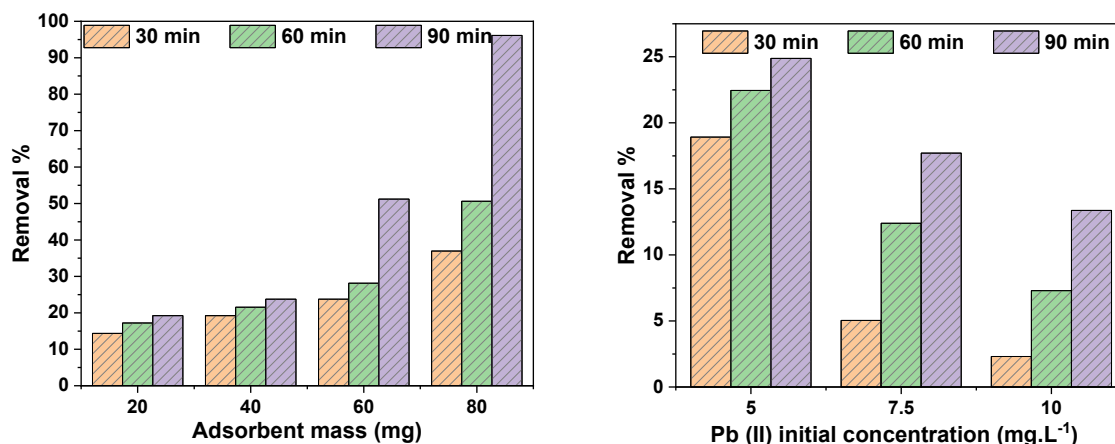


Fig. 12 (a) Removal % of Pb (II), studied at room temperature, in the presence of different amounts of $Mg_{0.33}Ni_{0.33}Co_{0.33}Sm_{0.01}Fe_{1.99}O_4$ nanoparticles and (b) effect of initial Pb (II) concentration on the removal % in the presence of $Mg_{0.33}Ni_{0.33}Co_{0.33}Sm_{0.01}Fe_{1.99}O_4$ nanoparticles.

additional adsorption sites acquired as the amount of nanoparticles increases.

Effect of Pb (II) initial concentration

The effect of Pb (II) initial concentration on the adsorption efficiency of $Mg_{0.33}Ni_{0.33}Co_{0.33}Sm_{0.01}Fe_{1.99}O_4$ nanoparticles was studied. Thus, 5, 7.5, and 10 $\text{mg}\cdot\text{L}^{-1}$ of Pb (II) solution was mixed with 40 mg of $Mg_{0.33}Ni_{0.33}Co_{0.33}Sm_{0.01}Fe_{1.99}O_4$ nanoparticles. As displayed in Fig. 12 (b), the removal % decreases with increasing the Pb initial concentration. The highest removal % was achieved in a 5 $\text{mg}\cdot\text{L}^{-1}$ Pb (II) solution. At low Pb (II) concentration, the availability of adsorption sites is relatively high. Thus, Pb (II) ions can be easily removed by

adsorption. Whereas, as the Pb (II) concentration increases, the available adsorption sites of $Mg_{0.33}Ni_{0.33}Co_{0.33}Sm_{0.01}Fe_{1.99}O_4$ adsorbent are limited which in turn decreases the removal %.

CONCLUSION

$Mg_{0.33}Ni_{0.33}Co_{0.33}Sm_xFe_{2-x}O_4$ nanoparticles were successively prepared by the co-precipitation method and used as adsorbents for the removal of heavy metal ions. XRD analysis reveals the purity and spinel structure of the prepared samples. The TEM image displays that the nanoparticles have a spherical morphology with an average particle size that ranges between 21.66 and 28.72 nm. An increase in the bandgap energy and a decrease in the Urbach energy was noticed upon Sm-doping.

Doping nanoparticles with Sm improved the adsorption efficiency for the removal of As (III) and Pb (II). The adsorption of As (III) follows the second-order kinetics. Among the applied adsorption isotherms, the Langmuir model best fits the experimental data for the removal of As (III). Additionally, the optimum adsorbent amount of $Mg_{0.33}Ni_{0.33}Co_{0.33}Sm_{0.01}Fe_{1.99}O_4$ nanoparticles was 80 mg. As the Pb (II) concentration increases, the removal % decreases. This was owed to the reduction in the adsorption sites of $Mg_{0.33}Ni_{0.33}Co_{0.33}Sm_{0.01}Fe_{1.99}O_4$ nanoparticles at high Pb (II) concentration. The results restate the potential of ferrite nanoparticles for the removal of heavy metal ions from wastewater.

CONFLICT OF INTEREST

The authors hereby declare that there is no conflict of interest.

REFERENCES

- Mahmud, H.N.M.E., A.O. Huq, and R. binti Yahya, The removal of heavy metal ions from wastewater/ aqueous solution using polypyrrole-based adsorbents: a review. *Rsc Advances*, 2016. 6(18): p. 14778-14791. <https://doi.org/10.1039/C5RA24358K>
- Shokri, A. and K. Mahanpoor, Removal of ortho-toluidine from industrial wastewater by UV/TiO₂ process. 2016.
- Shokri, A., M. Salimi, and T. Abmatin, Employing photo Fenton and UV/ZnO processes for removing Reactive red 195 from aqueous environment. *Fresenius Environmental Bulletin*, 2017. 26(2-A): p. 1560-1565.
- Qasem, N.A., R.H. Mohammed, and D.U. Lawal, Removal of heavy metal ions from wastewater: A comprehensive and critical review. *Npj Clean Water*, 2021. 4(1): p. 36. <https://doi.org/10.1038/s41545-021-00127-0>
- Kanwar, V.S., et al., Phytoremediation of toxic metals present in soil and water environment: a critical review. *Environmental Science and Pollution Research*, 2020. 27: p. 44835-44860. <https://doi.org/10.1007/s11356-020-11461-0>
- Ince, M. and O.K. Ince, Heavy metal removal techniques using response surface methodology: water/wastewater treatment, in *Biochemical Toxicology-Heavy Metals and Nanomaterials*. 2019, IntechOpen. <https://doi.org/10.5772/intechopen.88915>
- Peng, H. and J. Guo, Removal of chromium from wastewater by membrane filtration, chemical precipitation, ion exchange, adsorption electrocoagulation, electrochemical reduction, electrodialysis, electrodeionization, photocatalysis and nanotechnology: a review. *Environmental Chemistry Letters*, 2020. 18: p. 2055-2068. <https://doi.org/10.1007/s10311-020-01058-x>
- Tahir, M.B., H. Kiran, and T. Iqbal, The detoxification of heavy metals from aqueous environment using nano-photocatalysis approach: a review. *Environmental Science and Pollution Research*, 2019. 26(11): p. 10515-10528. <https://doi.org/10.1007/s11356-019-04547-x>
- Chai, W.S., et al., A review on conventional and novel materials towards heavy metal adsorption in wastewater treatment application. *Journal of Cleaner Production*, 2021. 296: p. 126589. <https://doi.org/10.1016/j.jclepro.2021.126589>
- Rajabi, M., et al., Comparison and interpretation of isotherm models for the adsorption of dyes, proteins, antibiotics, pesticides and heavy metal ions on different nanomaterials and non-nano materials-a comprehensive review. *Journal of Nanostructure in Chemistry*, 2023. 13(1): p. 43-65. <https://doi.org/10.1007/s40097-022-00509-x>
- Tamjidi, S., H. Esmaeili, and B.K. Moghadas, Application of magnetic adsorbents for removal of heavy metals from wastewater: a review study. *Materials Research Express*, 2019. 6(10): p. 102004. <https://doi.org/10.1088/2053-1591/ab3ffb>
- Jayalakshmi, R., J. Jeyanthi, and K.A. Sidhaarth, Versatile application of cobalt ferrite nanoparticles for the removal of heavy metals and dyes from aqueous solution. *Environmental Nanotechnology, Monitoring & Management*, 2022. 17: p. 100659. <https://doi.org/10.1016/j.enmm.2022.100659>
- Shokri, A., Using NiFe₂O₄ as a nano photocatalyst for degradation of polyvinyl alcohol in synthetic wastewater. *Environmental Challenges*, 2021. 5: p. 100332. <https://doi.org/10.1016/j.envc.2021.100332>
- Saghi, M., et al., The photo degradation of methyl red in aqueous solutions by α -Fe₂O₃/SiO₂ nano photocatalyst. *Journal of Nanoanalysis*, 2018. 5(3): p. 163-170.
- Shokri, A., Photocatalytic degradation of nitrotoluene in synthetic wastewater by CoFe₂O₄/SiO₂/TiO₂ nanoparticles using Box-Behnken experimental design. *DESALINATION AND WATER TREATMENT*, 2022. 247: p. 92-99. <https://doi.org/10.5004/dwt.2022.28037>
- Zahid, M., et al., Metal ferrites and their graphene-based nanocomposites: synthesis, characterization, and applications in wastewater treatment. *Magnetic Nanostructures: Environmental and Agricultural Applications*, 2019: p. 181-212. https://doi.org/10.1007/978-3-030-16439-3_10
- Khoso, W.A., et al., Synthesis, characterization and heavy metal removal efficiency of nickel ferrite nanoparticles (NFN's). *Scientific Reports*, 2021. 11(1): p. 3790. <https://doi.org/10.1038/s41598-021-83363-1>
- Punia, P., et al., Adsorption of Cd and Cr ions from industrial wastewater using Ca doped Ni-Zn nanoferrites: synthesis, characterization and isotherm analysis. *Ceramics International*, 2022. 48(13): p. 18048-18056. <https://doi.org/10.1016/j.ceramint.2022.02.234>
- Jadhav, S.A., et al., Rare earth-doped mixed Ni-Cu-Zn ferrites as an effective photocatalytic agent for active degradation of Rhodamine B dye. *Journal of Rare Earths*, 2023. <https://doi.org/10.1016/j.jre.2023.03.004>
- Taneja, S., et al., Nanostructured Rare Earth Nd³⁺-doped Nickel-Zinc-Bismuth Spinel Ferrites: Structural, Electrical and Dielectric Studies. *Ceramics International*, 2022. 48(19): p. 27731-27738. <https://doi.org/10.1016/j.ceramint.2022.06.073>
- Kirchberg, K., et al., Stabilization of monodisperse, phase-pure MgFe₂O₄ nanoparticles in aqueous and nonaqueous media and their photocatalytic behavior. *The Journal of Physical Chemistry C*, 2017. 121(48): p. 27126-27138. <https://doi.org/10.1021/acs.jpcc.7b08780>

22. Naik, C.C. and A. Salker, Structural, magnetic and dielectric properties of Dy³⁺ and Sm³⁺ substituted Co-Cu ferrite. *Materials Research Express*, 2019. 6(6): p. 066112. <https://doi.org/10.1088/2053-1591/ab0dd0>
23. Liu, Z., et al., Doping effect of Sm³⁺ on magnetic and dielectric properties of Ni-Zn ferrites. *Ceramics International*, 2017. 43(1): p. 1449-1454. <https://doi.org/10.1016/j.ceramint.2016.10.112>
24. Zhou, X., J. Wang, and D. Yao, Effect of rare earth doping on magnetic and dielectric properties of NiZnMn ferrites. *Journal of Alloys and Compounds*, 2023. 935: p. 167777. <https://doi.org/10.1016/j.jallcom.2022.167777>
25. Wu, X., et al., Effect of the rare-earth substitution on the structural, magnetic and adsorption properties in cobalt ferrite nanoparticles. *Ceramics International*, 2016. 42(3): p. 4246-4255. <https://doi.org/10.1016/j.ceramint.2015.11.100>
26. Hashim, M., et al., Influence of samarium doping on structural, elastic, magnetic, dielectric, and electrical properties of nanocrystalline cobalt ferrite. *Applied Physics A*, 2021. 127(7): p. 526. <https://doi.org/10.1007/s00339-021-04686-4>
27. Basma, H., et al., Enhancement of the magnetic and optical properties of Ni_{0.5}Zn_{0.5}Fe₂O₄ nanoparticles by ruthenium doping. *Applied Physics A*, 2022. 128(5): p. 409. <https://doi.org/10.1007/s00339-022-05552-7>
28. Chavan, P. and L. Naik, Investigation of energy band gap and conduction mechanism of magnesium substituted nickel ferrite nanoparticles. *physica status solidi (a)*, 2017. 214(9): p. 1700077. <https://doi.org/10.1002/pssa.201700077>
29. Palaniappan, P., N. Lenin, and R. Uvarani, Copper substitution effect on the structural, electrical, and magnetic properties of manganese and lanthanum (Mn_{1-x}Cu_xLa_{0.1}Fe_{1.9}O₄) nanoferrites. *Journal of Alloys and Compounds*, 2022. 925: p. 166717. <https://doi.org/10.1016/j.jallcom.2022.166717>
30. Lemziouka, H., et al., Synthesis, structural, optical and dispersion parameters of La-doped spinel zinc ferrites ZnFe₂-xLa_xO₄ (x= 0.00, 0.001, 0.005, 0.01 and 0.015). *Vacuum*, 2020. 182: p. 109780. <https://doi.org/10.1016/j.vacuum.2020.109780>
31. Ali, M., O. Hemeda, and A. Henaish, Tailoring changes in the physical, structural and linear optical properties of SrCuTi₂Fe₁₄O₂₇ W-type hexaferrite-doped PVA polymeric composite films. *Journal of Materials Science: Materials in Electronics*, 2021. 32(12): p. 16038-16051. <https://doi.org/10.1007/s10854-021-06153-5>
32. Faramawy, A., et al., Structural, Optical, Magnetic and Electrical Properties of Sputtered ZnO and ZnO: Fe Thin Films: The Role of Deposition Power. *Ceramics*, 2022. 5(4): p. 1128-1153. <https://doi.org/10.3390/ceramics5040080>
33. Massoudi, J., et al., Magnetic and spectroscopic properties of Ni-Zn-Al ferrite spinel: from the nanoscale to microscale. *RSC advances*, 2020. 10(57): p. 34556-34580. <https://doi.org/10.1039/D0RA05522K>
34. Tanbir, K., et al., Effect of doping different rare earth ions on microstructural, optical, and magnetic properties of nickel-cobalt ferrite nanoparticles. *Journal of Materials Science: Materials in Electronics*, 2020. 31: p. 435-443. <https://doi.org/10.1007/s10854-019-02546-9>
35. Chowdhury, S.R. and E.K. Yanful, Arsenic and chromium removal by mixed magnetite-maghemite nanoparticles and the effect of phosphate on removal. *Journal of environmental management*, 2010. 91(11): p. 2238-2247. <https://doi.org/10.1016/j.jenvman.2010.06.003>
36. Zhao, B., et al., Preparation of acrylamide/acrylic acid cellulose hydrogels for the adsorption of heavy metal ions. *Carbohydrate polymers*, 2019. 224: p. 115022. <https://doi.org/10.1016/j.carbpol.2019.115022>
37. Wekoye, J.N., et al., Kinetic and equilibrium studies of Congo red dye adsorption on cabbage waste powder. *Environmental Chemistry and Ecotoxicology*, 2020. 2: p. 24-31. <https://doi.org/10.1016/j.enccco.2020.01.004>
38. Masinga, T., M. Moyo, and V.E. Pakade, Removal of hexavalent chromium by polyethyleneimine impregnated activated carbon: Intra-particle diffusion, kinetics and isotherms. *Journal of materials research and technology*, 2022. 18: p. 1333-1344. <https://doi.org/10.1016/j.jmrt.2022.03.062>
39. Matouq, M., et al., The adsorption kinetics and modeling for heavy metals removal from wastewater by Moringa pods. *Journal of Environmental Chemical Engineering*, 2015. 3(2): p. 775-784. <https://doi.org/10.1016/j.jece.2015.03.027>
40. Umeh, T.C., J.K. Nduka, and K.G. Akpomie, Kinetics and isotherm modeling of Pb (II) and Cd (II) sequestration from polluted water onto tropical ultisol obtained from Enugu Nigeria. *Applied Water Science*, 2021. 11(4): p. 1-8. <https://doi.org/10.1007/s13201-021-01402-8>
41. Naseem, K., et al., Adsorptive removal of heavy metal ions using polystyrene-poly(N-isopropylmethacrylamide-acrylic acid) core/shell gel particles: adsorption isotherms and kinetic study. *Journal of Molecular Liquids*, 2019. 277: p. 522-531. <https://doi.org/10.1016/j.molliq.2018.12.054>
42. Goswami, A., P. Raul, and M. Purkait, Arsenic adsorption using copper (II) oxide nanoparticles. *Chemical engineering research and design*, 2012. 90(9): p. 1387-1396. <https://doi.org/10.1016/j.cherd.2011.12.006>

